Oxidation and Corrosion Resistance of NiCr-Re and NiCr-Re-Al₂O₃ Materials Fabricated by Spark Plasma Sintering

Katarzyna Pietrzak [1,2], Agata Strojny-Nędza [1], Kamil Kaszyca [1], Ivan Shepa [3,4], Erika Mudra [3], Marek Vojtko [3], Jan Dusza [3], Vitaliy Antal [5], Jana Hovancova [6] and Marcin Chmielewski [1,*]

[1] Łukasiewicz Research Network Institute of Electronic Materials Technology, 133 Wolczynska Str., 01-919 Warsaw, Poland; katarzyna.pietrzak@itme.edu.pl (K.P.); agata.strojny@itme.edu.pl (A.S.-N.); kamil.kaszyca@itme.edu.pl (K.K.)

[2] Institute of Fundamental Technological Research, Polish Academy of Sciences, 5B Pawinskiego, 02-106 Warsaw, Poland

[3] Institute of Materials Research, Slovak Academy of Sciences, 47 Watsonova Str., 040 01 Košice, Slovakia; ishepa@saske.sk (I.S.); emudra@saske.sk (E.M.); mvojtko@saske.sk (M.V.); jdusza@saske.sk (J.D.)

[4] Faculty of Materials, Metallurgy and Recycling, Technical University of Kosice, Letna 9, 040 01 Kosice, Slovakia

[5] Institute of Experimental Physics of the Slovak Academy of Sciences, 47 Watsonova Str., 040 01 Kosice, Slovakia; antal@saske.sk

[6] Department of Physical Chemistry, P.J. Šafárik University in Košice, 11 Moyzesova Str., 040 01 Košice, Slovakia; jana.hovancova@student.upjs.sk

[*] Correspondence: marcin.chmielewski@itme.edu.pl; Tel.: +48-12-835-30-41 (ext. 415)

Abstract: The thermal and oxidation resistance of elements found in the combustion boilers of power generation plants are some of the most important factors deciding their effectiveness. This paper shows the experimental results of the influence of NiCr-based material composition on the microstructure and phase changes occurring during the oxidation and corrosion process. NiCr alloy was modified by the addition of rhenium and aluminum oxide. Materials were densified using the spark plasma sintering method at a sintering temperature of 1050 °C. Oxidation tests conducted up to 1100 °C under synthetic airflow revealed the formation of a thin Cr_2O_3 layer protecting the material against in-depth oxidation. Results of electrochemical corrosion in a 0.5 M NaCl solution indicated a positive role of Re and Al_2O_3 addition, confirmed by low corrosion current density values in comparison to the other reference materials. According to the provided positive preliminary test results, we can conclude that a NiCr-Re-Al₂O₃ system in coating form was successfully obtained by the plasma spraying method.

Keywords: NiCr; rhenium; aluminium oxide; metal matrix composites; oxidation; corrosion

1. Introduction

In power generation plants, especially those co-fired with biomass, the operating temperature is often limited to reduce severe chlorine-induced corrosion, solid particle erosion, and slagging, as these factors may cause unexpected plant shutdowns, along with high maintenance costs. Weld overlays are used at times to prevent corrosion of the boiler's steel tubes but this can be a costly solution. Alternatively, special coatings may be used to improve boilers' performance in highly corrosive combustion environments and extend its lifetime.

The main causes of boilers corrosion are: (i) the chemically aggressive environment connected with the fuel composition and combustion conditions, (ii) the heat exchanger operating temperature and exhaust gases temperature connected with the boiler structure, (iii) the properties of the structural materials used in boilers bearing in mind the "history" of working conditions. The most detrimental factors for boiler material durability are the attack of sulfur and chlorine due to their presence in the chemical composition of the fuel [1,2]. For example, if biomass and waste fuels are used their high chlorine content is the major trigger for severe chlorine-induced corrosion that may limit plant operating temperature and efficiency. To avoid this undesirable scenario the gas temperatures in the secondary superheaters of biomass co-fired plants are often reduced to ~600 °C, and steam temperatures are kept below 400 °C. Fly ash particles entrained in the outlet gas from boiler furnaces can also cause erosive wear on steel surfaces along the downstream flow path [3].

The most frequently used materials for heat exchanger surfaces in power plant boilers, such as superheaters, are Ni-Cr alloys [4]. Ni-Cr alloys show high hot corrosion resistance under the use conditions due to the formation of oxides of chromium and spinels, which may block the diffusion of degrading species [5]. They can be also applied as thin films for precision resistors [6] or solid oxide fuel cell (SOFC) interconnections [7].

A promising alternative to metallic coatings is less expensive hybrid coatings based on oxides or carbides. Among commercially available materials recommended for combustion boiler protection, the following ones are often used: NiCr, NiCrTi, NiCrSi, NiCrMo, NiCrAl, NiCr-Cr_3C_2, special steels, and Inconel alloys [8–14]. The mentioned materials manifest good resistance to solid particle impingement erosion, high-temperature chlorine-sulfur corrosion, and thermal shocks. They maintain their protective properties up to 900 °C and are characterized by good adhesion to substrates, forming entirely sealed systems with continuous and stable microstructure [15]. Additionally, a dense and well-adhered coating structure is of crucial importance, as well as the ability to form a protective oxide layer and sufficient mechanical properties are needed for enhanced corrosion protection performance. However, the constantly growing technical requirements necessitate searching for new materials to enable boiler operation in higher temperature regimes for longer times.

From this point of view, oxidation and corrosion resistance become an extremely important issue. A lot of works have been published on the effect on the isothermal oxidation [16,17] and corrosion resistance [18–20] of Ni-based alloys. Many different alloying elements, like Nb, C, Ti, W, Re, etc. have been tested to determine how they influence material resistivity. For example, the authors of [17] confirmed that the oxidation resistance of Ni-Fe-Cr alloy is greatly affected by carbide precipitates. In the case of single-crystal Ni-based superalloy oxidized at 900, 1000, and 1100 °C [16] it was found that small addition of Re caused an increase of the Al microsegregation degree between the dendritic and interdendritic areas and induced non-uniform oxidation of the alloy.

The same occurs in the case of the corrosion resistance of Ni-Cr alloys. In [18] corrosion tests of Ni-30Cr alloy were carried out in an Ar, CO_2 and O_2 atmosphere at 650 °C during 50, 150, and 310 h. The result of the high-temperature exposure was the formation of a continuous Cr_2O_3 layer, with local outer NiO islands. A three- layered structure consisting of $(Ni,Fe)_3O_4$ spinel, $(Ni,Fe,Cr)_3O_4$ spinel, and Cr_2O_3 was identified as a result of corrosion tests of Ni-Fe-Cr alloy after treatment at 950 °C in a molten cryolite-based mixture.

The combination of environmental conditions to which materials are exposed during operation in power boilers forces the search for new, durable, and resistant to various factors (atmosphere, temperature, other) material solutions.

Rhenium addition to the presently used materials for high-temperature applications can be beneficial as shown by our preliminary research [21]. This metal has a very high melting point (3186 °C) and high thermal stability and it is characterized by high hardness. Rhenium has a range of uses in modern technological solutions, such as catalysts, thermal elements, semiconductor electrodes, turbine blades, etc. [22–24]. Due to its very high density (21.2 g/cm^3), but also limited availability and high price, its use in designed composite materials should be reduced to a small addition, sufficient to achieve the intended effect. The influence of rhenium addition on the microstructure and

properties (physical, mechanical) of different nickel-based alloys has been the subject of many scientific reports [25–29]. Generally, the obtained results indicate its positive effects, hence the potential range of rhenium applicability is still evolving.

At the same time, the search for the most suitable technologies for the production of materials containing high-melting components is being conducted. Spark plasma sintering (SPS) is a promising method for the fabrication of advanced materials for high-temperature applications. SPS is a powder metallurgy technique, in which a loose or loosely bonded powder is consolidated (sintered) under applied pressure at an elevated temperature (below the melting point) induced by an electric current. SPS is understood as a complex multiphysics process. Its effectiveness is related to the interaction of electrical, thermal, and mechanical phenomena. The main advantage of SPS resulting from the short process time is related to the possibility of sintering materials without significant grain growth. Additionally, it is possible to produce near-net-shape bulk materials from powders with reduced cycle times. This can be used for manufacturing a wide spectrum of materials such as metals, alloys, intermetallics, ceramics, metal and intermetallic-ceramic matrix composites, functionally graded materials, graphite-containing materials and many others [30–32]. For instance, in aero engines by adding small admixtures of rhenium to Ni-based superalloys for turbine blades a profound effect was achieved with regard to hardness, strength, and corrosion resistance of the alloy [33].

This work is dedicated to the preparation of NiCr-based materials and the effect of the Re and Al$_2$O$_3$ addition on the materials' properties. The characterization of the modified systems concentrates on the analysis of their microstructure, high-temperature oxidation, and electrochemical corrosion resistance characterization. The presented results constitute part of our preliminary work prior to the development of protective layers intended for covering structural elements of power boilers exposed to high temperatures and an aggressive working environment.

2. Materials and Methods

2.1. Samples Preparation

Gas atomized 80Ni-20Cr powder (Oerlikon Metco-Amdry) with a nominal composition of 79.5Ni-19.3Cr-0.13Fe-0.32Mn-0.72Si (in wt.%) and mean particle size of 45 μm was used as basic material. Rhenium (KGHM) and electrocorundum (KOS) powders of 99.7% purity and with the mean particle size of 5 μm and 4 μm, respectively, were applied to modify the chemical composition of NiCr alloy.

The following materials composition were prepared (in vol.%): (i) 100NiCr, (ii) 99NiCr-1Re, (iii) 90(99NiCr-1Re)-10Al$_2$O$_3$. High energy milling of NiCr powder with rhenium and electrocorundum Al$_2$O$_3$ addition was performed for 4 h of each admixing process, using a planetary ball mill (Fritsch Pulverisette 6, Idar-Oberstein, Germany) with tungsten carbide balls as grinding medium. A ball-to-powder weight ratio of 5:1 and a 100 rpm rotational speed was adopted.

The ball-milled powder mixtures were consolidated using the spark plasma sintering technique. The cylindrical graphite dies with an inner diameter of 26 mm and an outer diameter of 50 mm were used. The inner surface of the die and radial surfaces of the punches were covered with a graphite foil (0.5 mm in thicknesses) to facilitate the removal of the sintered specimens. The die was wrapped in graphite felt (with a thickness of 5 mm) to minimize heat loss by thermal radiation.

After the preliminary tests the following sintering conditions were chosen: (i) sintering temperature: 1050 °C, (ii) heating rate: 100 °C/min, (iii) holding time: 10 min, (iv) external pressure: 50 MPa, (v) atmosphere: vacuum, 5×10^{-5} mbar.

The final product was obtained in the form of disks with 25 mm in diameter and 5 mm thick. Densities of the sintered materials were measured using the hydrostatic method based on the Archimedes' Principle. Evaluation of the bulk density of a specimen with an arbitrary porosity is based on the measurements (using a laboratory scale, Mettler Toledo) of the mass of the dry specimen, m_s, the mass of the specimen saturated with water m_n and the weight of the liquid

saturated specimen suspended in the water, m_w. Then, the bulk density ρ of the specimen with all kind of porosity is calculated from the following formula:

$$\rho = \frac{m_s}{m_n - m_w} \times \rho_f \tag{1}$$

where: ρ_f is the density of the fluid at the measurement temperature.

The morphologies of NiCr based powder mixtures and sintered composites were characterized by a SEM-Dual-Beam SEM/FIB ZEISS AURIGA Compact system (Zeiss, Oberkochen, Germany) coupled with an energy-dispersive x-ray spectroscopy (EDX) detector (Bruker, Billerica, MA, USA). To reveal the structure of the prepared samples common polishing procedure was applied.

2.2. Thermal Oxidation Tests

Differential scanning calorimetry and thermogravimetry measurements (DSC/TG) of the sintered materials were used for the determination of the oxidation resistance. The combination of these two measuring techniques is suitable for the characterization of the thermal behavior of the material, particularly in the oxidative atmosphere. DSC/TG measurements were simultaneously performed from 35 °C up to 1100 °C under synthetic airflow (50 mL/min) with a heating rate of 10 °C/min using standard Al_2O_3 crucibles. DSC/TG calibration and baseline were used for correct measurements of the samples. After the oxidation test, SEM/EDX and Raman spectroscopy were applied to analyze the chemical transformations on the surface of the material.

2.3. Electrochemical Corrosion Tests

The electrochemical measurements were carried out using an Autolab MAC90166 (Metrohm, Herisau, Switzerland). The measurements were conducted in a three-electrode system with an Ag/AgCl/KCl (3 M) reference electrode, a platinum counter electrode, and an alloy sample as the working electrode. Corrosion was studied in a 0.5 M NaCl solution. The electrochemical polarization was carried out from −800 mV to −100 mV (vs. Ag/AgCl/KCl 3 M) at a polarization scan rate of 1 mV/s.

The corrosion behavior of the prepared alloy samples was studied by the anodic polarization method in the 0.5 M NaCl solution at the laboratory temperature (25 °C). Representative polarization curves (Tafel plots) for the samples were used for calculation of the most important corrosion parameters.

As the reference material chrome-molybdenum steel 16Mo3 (with the following chemical composition: 0.12–0.20 C, 0.35 Si, 0.4–0.9 Mn, 0.025 P, 0.01 S, 0.3 Cr, 0.25–0.35 Mo, 0.3 Ni, 0.012 N, 0.3 Cu, Fe balance) was tested.

3. Results and Discussion

The morphologies of NiCr based powder mixtures characterized by SEM/EDX are presented in Figure 1. The as-received NiCr alloyed powders are typically spherical, whereas the rhenium and Al_2O_3 powders are irregular with sharp edges. No significant changes in the morphology of powders were observed following high energy ball milling. Rhenium particle distribution was uniform throughout the whole volume of the mixture. The smaller Re particles decorate the surface of NiCr spheres. It can be stated that they are permanently mechanically bound to NiCr particles. The following subsequent mixing process with the addition of electrocorundum introduces small changes in the system. Similarly, the Al_2O_3 particles are located on the surface of the larger NiCr ones; however, some of the loose (not connected) powder is visible in the SEM micrographs.

The densities of the sintered composites are presented in Table 1. For the assumed volume fractions, the theoretical densities of the composites were defined using the density of nickel-chromium alloy ρ_{NiCr} = 8.50 g/cm³, rhenium ρ_{Re} = 21.06 g/cm³ and aluminum oxide ρ_{Al2O3} = 3.97 g/cm³. The results show the average density estimated for 5 measurements of each of the five samples in a given measurement series. As can be seen almost fully dense materials with a small difference in relative density depending on the chemical composition were obtained.
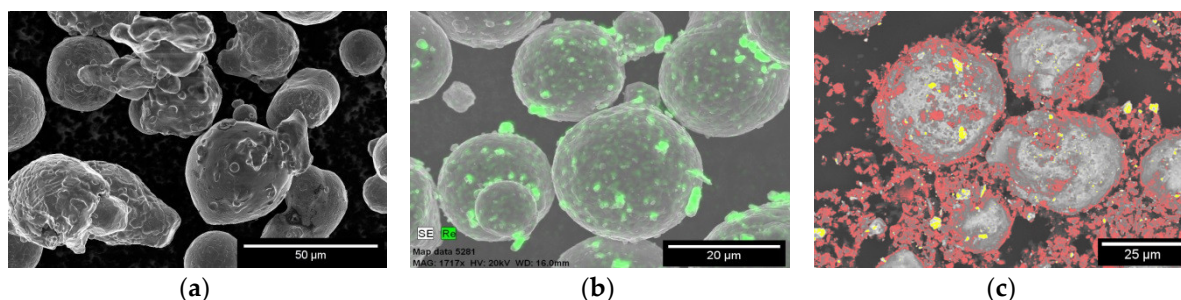
Figure 1. SEM and EDX micrographs of powders used for sintering process: (**a**) 100NiCr, (**b**) 99NiCr-1Re (green color refers to Re), (**c**) 90(99NiCr-1Re)-10Al$_2$O$_3$ (yellow color refers to Re, and red-to Al$_2$O$_3$).

Table 1. Densities of the NiCr based materials sintered at 1050°C by SPS.

Material Composition	Theoretical Density (g/cm³)	Measured Density (g/cm³)	Relative Density (%)
NiCr	8.50	8.42	99.1 ± 0.2
NiCr-Re	8.62	8.52	98.8 ± 0.3
NiCrRe-Al$_2$O$_3$	8.16	8.08	99.0 ± 0.2

Microstructural characterization of the sintered samples was also performed utilizing SEM and EDX. The captured images of the microstructure are presented in Figure 2. To reveal the structure of the prepared samples common polishing procedure was applied.
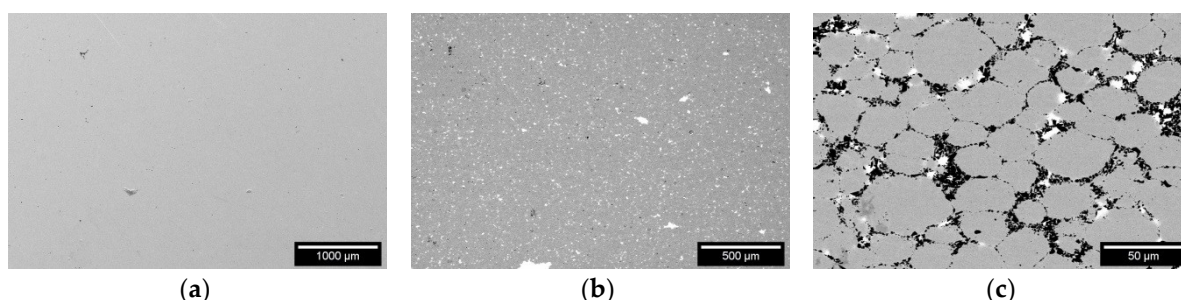

Figure 2. SEM images of the polished sintered samples: (**a**) 100NiCr, (**b**) NiCr-Re, and (**c**) NiCr-1Re-Al$_2$O$_3$.

Detailed elemental analyses of 90(99NiCr-1Re)-10Al$_2$O$_3$ composite structure were performed by the EDX method and visualized for each element in Figure 3.
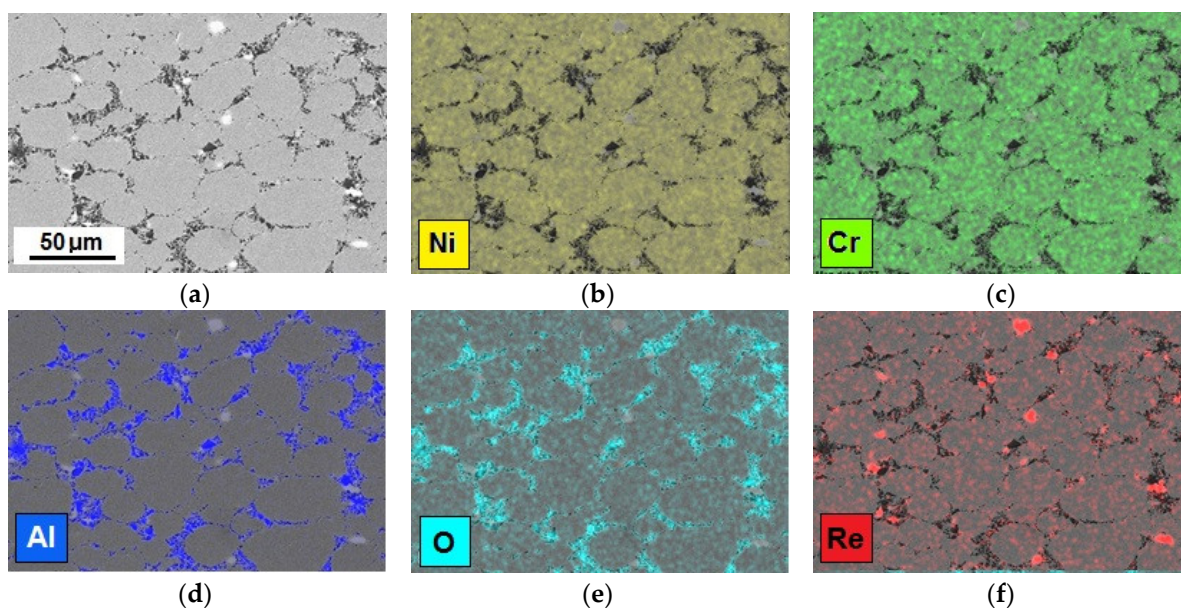
Figure 3. SEM micrograph (**a**) and EDX analysis (**b**–**f**) of the surface distribution of the elements (Ni, Cr, Al, O, Re) in the sintered NiCr-Re-Al$_2$O$_3$ composite material.

It should be noticed that in all examined cases it was obtained high densification level of sintered materials. In composite reinforced by electrocorrundum particles, the porosity exists in the area of the ceramic phase. Rhenium is uniformly distributed in the whole volume of the sintered samples. No evidence of rhenium dissolution in the NiCr alloy structure was found, as was the case with the sintering of rhenium and chromium-based composites [21].

DSC/TG curves for each sample are presented in Figure 4. Here the sample of 16Mo3 steel was used for a comparison with the experimental NiCr modified ones. 16Mo3 steel was chosen as a perspective substrate/carrier for the coatings based on NiCr alloys, due to its application. This kind of steel is commonly used in the construction of key elements of power boilers, including steam separators. During the thermal tests, it showed much lower oxidation resistance than the prepared NiCr systems. Thermal oxidation process on the surface of this steel may be divided into the two stages different by rates (determined from the curve slope): first stage—low-temperature slow oxidation process with an onset at 747 °C continued with the second stage—rapid oxidation process starting at above 940 °C. As can be seen from the TG curves measured for the NiCr based materials, any mass losses or gains were not detected. This means that in the temperature range of 35–1100 °C, sintered materials show excellent stability without any visible oxidation during the experiment performed in the synthetic airflow. DSC curves have a similar shape and slope, without any peaks characteristic for specific thermal events, what be referred to as the slight detector drift and sorbed gases or moisture evolution at the temperatures below 150 °C.
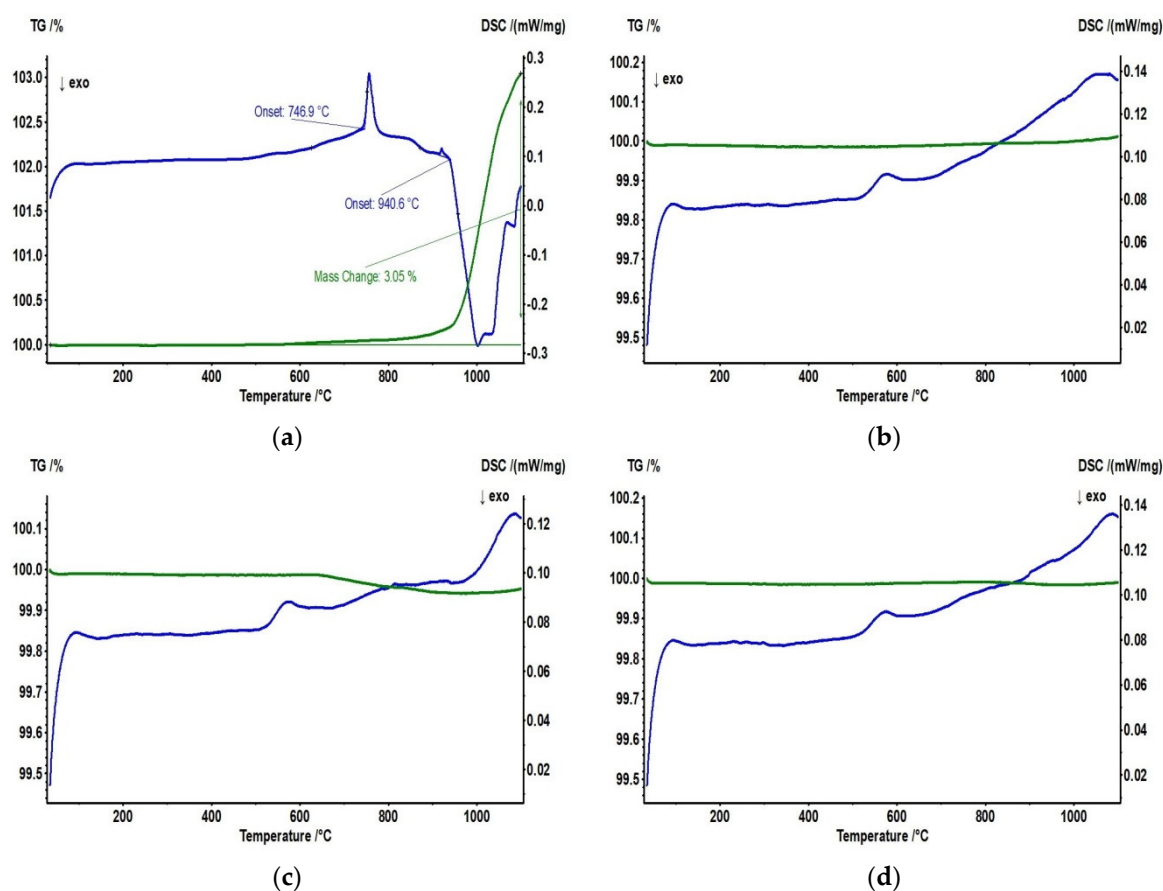

(**a**)

(**b**)

(**c**)

(**d**)

Figure 4. DSC/TG curves measured for the samples: (**a**) 16Mo3 steel, (**b**) pure NiCr, (**c**) NiCr-Re and (**d**) NiCr-Re-Al$_2$O$_3$.

Figure 5 shows the SEM images of the surface of the sample materials after the oxidation tests. In the NiCr and its modified samples, no signs of any thermally induced oxidation or degradation

are visible. The low-intensity peak at 550 °C on the DSC curve should be assigned to some internal process in the NiCr alloy, like diffusion or atom rearrangement, which does not imply mass changes. As can be seen from the TG curves, there is a slight weight loss recorded for the NiCr-Re as well as the NiCr-Re-Al$_2$O$_3$, samples starting at approx. 900 °C, which is less than 0.05 wt.%. Before the measurements, the equipment was precisely calibrated and background curves were recorded. Such a low value is not quite reliable, because it is already on the edge of the detection capabilities, especially at the high temperatures, and perhaps results from some slight thermal drift of the detector, rather than any real values. As an exception, on the surface of the steel sample, the formation of the oxide layer is confirmed. The composition and nature of the oxide layer were investigated by Raman spectroscopy.
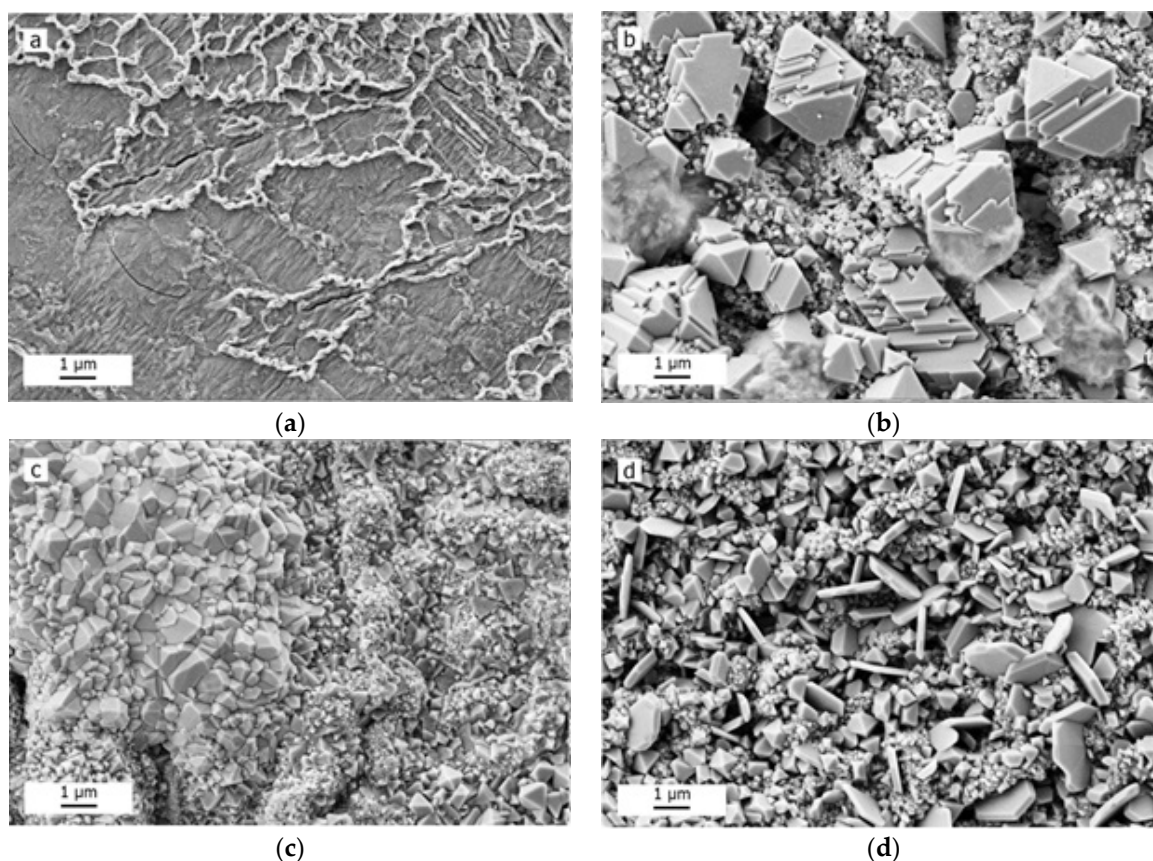

(**a**)

(**b**)

(**c**)

(**d**)

Figure 5. SEM micrographs of the surface of the samples after the oxidation resistance tests: (**a**) 16Mo3 steel, (**b**) pure NiCr, (**c**) NiCr-Re, and (**d**) NiCr-Re-Al$_2$O$_3$.

Raman spectroscopy measurements were performed on the samples before and after the oxidation resistance tests. Due to the low penetration ability and inability of metals to show Raman bands this technique is selectively sensitive to the impurities and oxides formed on the surface. It is a surface analysis technique, not sensitive to the underlying metals. Instead of elemental analysis, provided by EDX, it is capable of providing information about the chemical composition and nature of the substance (amorphous/crystalline) and its phase composition.

The Raman spectra in Figure 6a show wide and indistinct peaks recorded for the untreated samples, which refers to the amorphous or some semicrystalline oxide film on the surface. This also may be because insufficient contamination happened during the sample preparation. The low intensity of the recorded spectra due to insufficient amount of the Raman active sample (even at the long recording times and high intensity of the excitation laser) defines the low thickness of the films. Wide peak recorded at 1330 cm^{-1} for the 16Mo3 steel (Figure 6) refers to the semicrystalline hematite Fe$_2$O$_3$ (common forms during the sample preparation and storage).
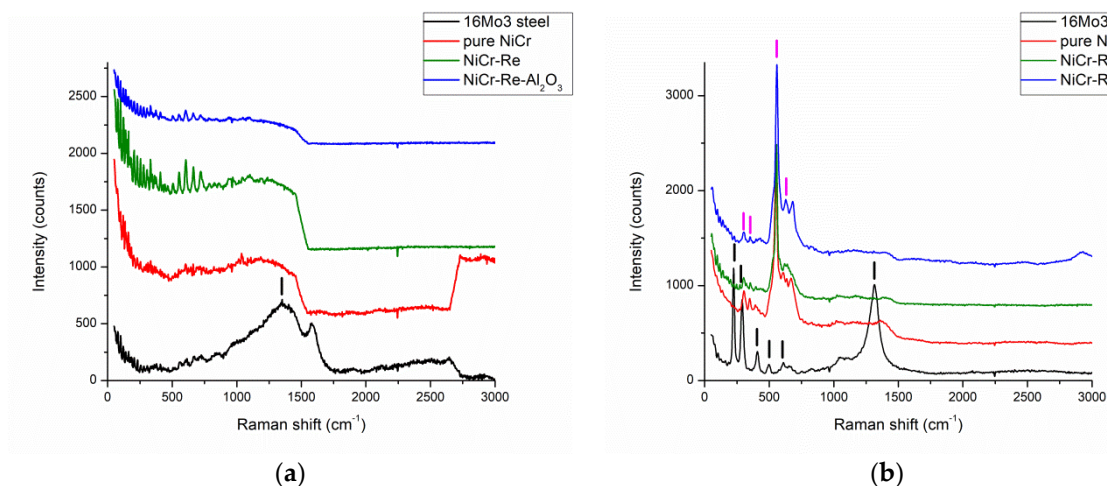
Figure 6. Raman spectra of (**a**) the samples before and (**b**) after the oxidation resistance tests.

Figure 6b depicts the Raman spectra recorded after the oxidation tests. As expected, hematite (Fe_2O_3) was found in relatively large amounts on the surface of the 16Mo3 steel (black line), due to its preferable formation during the oxidation in air. The presence of this type of iron oxide was definitely confirmed by Raman spectroscopy—sharp and high-intensity peaks characteristic peaks recorded at 226, 292, 411, 497, 610 (shift from 612), 1315 cm^{-1} (marked by black vertical lines on the spectra above).

The oxide layer on the surface of the pure NiCr (red line), NiCr-Re (green line), and NiCr-Re-Al_2O_3 (blue line) samples consist mostly of Cr_2O_3. This was confirmed by the analysis of spectra after the thermogravimetric measurements performed in air. Peaks measured at 300, 350, 560 (max intensity), and 615 cm^{-1} are characteristic for the Cr_2O_3 (marked on the spectra by dark magenta vertical lines). Formation of the oxide layers of the samples is one of the protection mechanisms providing the high oxidation and wear resistivity established for these composite materials in a dedicated layer form.

Experimental polarization curves (Figure 7) were measured for all the samples to estimate the corrosion potential (E_{corr}) and corrosion rate (j_{corr}). The values of E_{corr} vs. Ag/AgCl/KCl (3 M) and j_{corr} for the Tafel plots by using cathodic and anodic branches are listed in Table 2. A small scan rate (1 mV/s) was used to minimize the distortion effects in the Tafel slopes. The significant spikes in the case of prepared samples are caused by pitting initiation and repassivation. Similar behavior was reported in the literature [34].
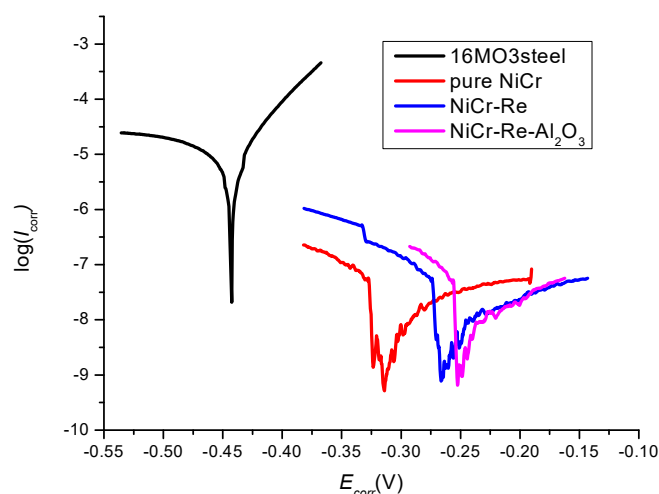

Figure 7. The experimental polarization curves for 16Mo3 steel (black curve), pure NiCr (red curve), NiCr-Re (blue curve), NiCr-Re-Al_2O_3 (pink curve).

Table 2. Results of the corrosion tests.

Material	E_{corr} (V)	j_{corr} (μA/cm²)	Reference
16Mo3 steel	−0.410	1.35	Reference material
pure NiCr	−0.296	0.0792	This work
NiCr-Re	−0.279	0.0455	This work
NiCr-Re-Al2O3	−0.253	0.0134	This work
Al-15%Mg2Si-1%Ni	−0.819	0.407	[35]
Ni-Cu alloy	−0.404	22.9	[36]
Ti38Ni38Cu12Zr12	−0.285	0.289	[37]
Ti42Ni42Cu8Zr8	−0.271	0.147	[37]
TiNi	−0.288	0.087	[38]
Diamond-like carbon/TiNi	−0.088	0.02	[39]
Plasma treated TiNi	−0.052	0.013	[40]
Ti-10Ni1.2	−0.076	1700	[41]

The reproducibility of Tafel curves was high what confirms the reliability and precision of the obtained results. Corrosion tests provide us with the following information: corrosion potential, corrosion current, and corrosion current density, polarization resistance, kinetic parameters, and corrosion rate (in mm per year). To calculate the current density, the sample's geometric surface area parameter was used. The corrosion potential (E_{corr} vs. Ag/AgCl/KCl (3 M)) and the corrosion current density (j_{corr}) were calculated from the intersection of the extrapolated anodic and cathodic Tafel lines.

The obtained results, presented in Table 2, confirm that the corrosion potential of the substrate steel is much more negative than that of NiCr alloys. Moreover, the corrosion current density of 16Mo3 steel is much higher. The corrosion current density is directly proportional to the corrosion rate – a lower value indicates better resistance against corrosion. Similarly, the more positive anodic corrosion potential represents a higher resistance against corrosion. According to this information, the most resistive one against corrosion is the NiCrRe-Al₂O₃ composition. NiCrRe-Al₂O₃ displays not only much more positive corrosion potential in comparison to the reference material, but also comparable potential values with other alloys listed in Table 2.

Due to the promising material characteristics of the bulk NiCrRe-Al₂O₃ composites from the above tests, it was decided to proceed with its deposition. The preliminary tests of preparing NiCrRe-Al₂O₃ coatings on steel substrates, having in mind their potential application in the energy generation industry as coatings for heat exchange elements in fluidal boilers, were performed by a plasma spraying method. The obtained coatings of about 500 μm in thickness were homogeneous across the specimen section and well-bonded to the steel substrate (Figure 8). Metal grains of the composite coating take the form of elongated flakes perpendicular to the direction of coating deposition. The identified porosity of the composite coatings was lower than 2%, which is acceptable for their application in fluidal bed combustion boilers. Rhenium and aluminum oxide particles were quite uniformly distributed in the whole layer. Some discontinuities at the layer/substrate area were noticed, which may affect the adhesion of the layer and its strength and durability. The detailed investigation of NiCrRe-Al₂O₃ layered materials will be the next step of our research in the nearest future.
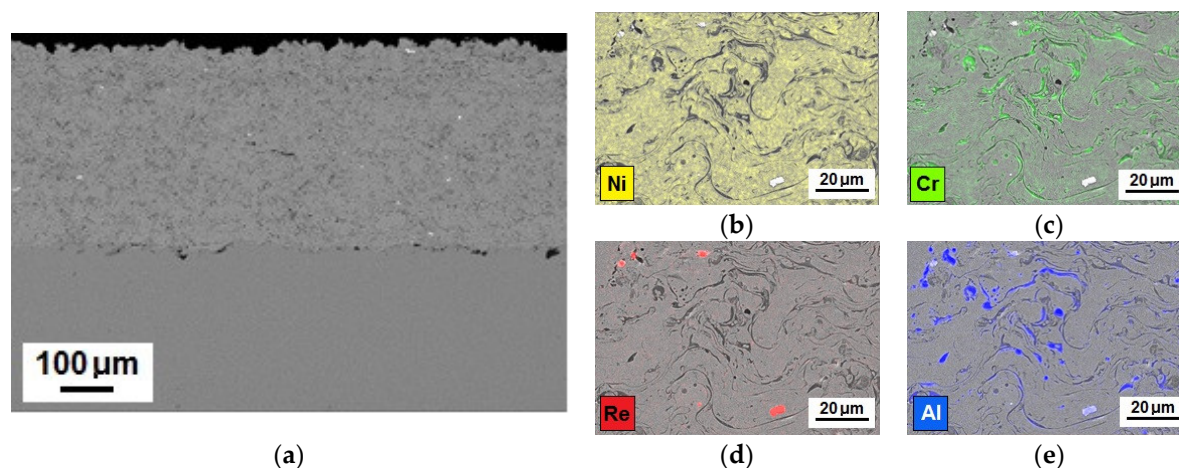
Figure 8. SEM micrograph (**a**) and EDX surface distribution of elements (Ni, Cr, Re, Al) analysis (**b**–**e**) of plasma-sprayed NiCrRe-Al$_2$O$_3$ coating deposited on 16Mo3 steel substrate.

The main goal of the research described in the paper was purely utilitarian – to obtain a material with the assumed functional properties. It was necessary to check and explain the physicochemical processes accompanying materials formation and their behavior in a severe oxidation and corrosion environment. The provided analysis allowed for faster attainment of the solution. From the point of view of the functional properties of the developed and tested materials, the fact that the obtained composites are characterized by an even distribution of Re and Al$_2$O$_3$ reinforcement in their entire volume and the stability of properties under service conditions looks very promising. The results of structural investigations show the uniform distribution of Re and Al$_2$O$_3$ particles on NiCr grains and creation of a structure similar in form to a spatial mesh. Such a structure should be favorable due to the thermal loads. Other crucial aspect is corrosion resistance. Thermodynamic analyzes and previous experimental work dedicated to Cr-Al$_2$O$_3$ composite materials confirms that formation of chromium oxides on the materials' surface that allow for its protection from further oxidation [42]. This allows for prospective applications of the layered technology in practical use.

4. Conclusions

The paper presents the experimental results of resistance to oxidation and corrosion of sintered materials based on NiCr alloys. It was confirmed that its modification by rhenium and aluminum oxide resulted in improved thermal oxidation and electrochemical corrosion resistance, compared to pure 16Mo3 steel and the unmodified NiCr basic alloy. Microstructural analyses showed the high density of the sintered materials with quite uniform distribution of reinforcements (rhenium and aluminium oxide) in the whole volume. Based on the oxidation tests it can be stated that in all three types of NiCr-based materials the thin protective layer of chromium oxide (Cr$_2$O$_3$) was formed, in contrast to a steel substrate, where rapid oxidation occurs over 750 °C resulting in the creation of relatively large amounts of hematite (Fe$_2$O$_3$), as confirmed by Raman spectroscopy. Estimated values of corrosion potential (E_{corr}) and the corrosion current density (j_{corr}) indicate the NiCr-Re-Al$_2$O$_3$ material as the most resistant to corrosion in 0.5 M NaCl solution. Further work will be focused on developing a technology for deposition of NiCr-Re-Al$_2$O$_3$ coatings as the most favorable for application in combustion boilers.

Author Contributions: Conceptualization, K.P., J.D., M.C.; methodology, K.P., J.D., M.C.; materials preparation, K.K., A.S.-N., M.C.; investigation, I.S., E.M., M.V., V.A., J.H., and A.S.-N.; writing—original draft preparation, K.P., I.S., M.C.; writing—review and editing, K.P., I.S., M.C.; visualization, I.S., K.K. All authors have read and agreed to the published version of the manuscript. All authors have read and agreed to the published version of the manuscript.

Conflicts of Interest: The authors declare no conflict of interest.

References

1.   Ghosh, D.; Mitra, S.K. High temperature corrosion problem of boiler components in presence of sulfur and alkali based fuels. *High Temp. Mater. Proc.* **2011**, *30*, 81–85.

2.   Azamata, O.D.; Jibatswen, T.Y.; Michael, O.C. Effect of chlorine and sulphur on stainless steel (AISI 310) due to high temperature corrosion. *Am. J. Eng. Res.* **2016**, *5*, 266–270.

3.   Nagarajan, R.; Ambedkar, B.; Gowrisankar, S.; Somasundaram, S. Development of predictive model for fly-ash erosion phenomena in coal-burning boilers. *Wear* **2009**, *267*, 122–128.

4.   Morks, M.F.; Berndt, C.C. Corrosion and oxidation properties of NiCr coatings sprayed in presence of gas shroud system. *Appl. Surf. Sci.* **2010**, *256*, 4322–4327.

5.   Oksa, M.; Metsajoki, J. Optimizing NiCr and FeCr HVOF coating structures for high-temperature corrosion protection applications. *J. Therm. Spray Technol.* **2015**, *24*, 436–453.

6.   Lee, B.J.; Shin, P.K. Fabrication and characterization of Ni-Cr alloy thin films for application to precision thin film resistors. *J. Electr. Eng. Technol.* **2007**, *2*, 525–531.

7.   Yang, Z.; Xia, G.G.; Stevenson, J.W. Evaluation of Ni–Cr-base alloys for SOFC interconnect applications. *J. Power Sources* **2006**, *160*, 1104–1110.

8.   Hamatani, H.; Shimoda, N.; Kitaguchi, S. Effect of the composition profile and density of LPPS sprayed functionally graded coating on the thermal shock resistance. *Sci. Technol. Adv. Mat.* **2003**, *4*, 197–203.

9.   Uusitalo, M.A.; Vuoristo, P.M.J.; Mantyla, T.A. High-temperature corrosion of coatings and boiler chlorine-containing atmosphere. *Surf. Coat. Technol.* **2002**, *161*, 275–285.

10. Matthews, S.; James, B.; Hyland, M. High-temperature erosion of Cr3C2-NiCr thermal spray coatings - The role of phase microstructure. *Surf. Coat. Technol.* **2009**, 203, 1144–1153.

11. Zhang, Y.J.; Sun, X.F.; Guan, H.R.; Hu, Z.Q. 1050 °C isothermal oxidation behavior of detonation gun sprayed NiCrAlY coating. *Surf. Coat. Technol.* **2002**, *161*, 302–305.

12. Omoniyi, F.; Olubambi, P.; Sadiku, E. High-temperature oxidation resistance of Ni22Cr11Al bond coat produced by spark plasma sintering as thermal barrier coatings. *J. Mater. Sci. Eng.* **2016**, *5*, 1000236.

13. Chmielewski, T.; Siwek, P.; Chmielewski, M.; Piątkowska, A.; Grabias, A.; Golański, D. Structure and selected properties of arc sprayed coatings containing in-situ fabricated Fe-Al intermetallic phases. *Metals* **2018**, *8*, 1059.

14. Sartowska, B.; Piekoszewski, J.; Waliś, L., Senatorski, J.; Stanisławski, J.; Ratajczak, R.; Nowicki, L.; Kopcewicz, M.; Prokert, F.; Barlak, M. Structural and tribological properties of carbon steels modified by plasma pulses containing inert and active ions. *Surf. Coat. Technol.* **2007**, *201*, 8295–8298.

15. Plasma System. Available online: https://www.plasmasystem.pl/en/shells/highresist (accessed on 24 July 2020).

16. Huang, L.; Sun, X.F.; Guan, H.R.; Hu, Z.Q. Effect of rhenium addition on isothermal oxidation behavior of single-crystal Ni-based superalloy. *Surf. Coat. Technol.* **2006**, *200*, 6863–6870.

17. Wei, W.; Geng, S.; Xie, D.; Wang, F. High temperature oxidation and corrosion behaviours of Ni-Fe-Cr alloys as inert anode for aluminum electrolysis. *Corros. Sci.* **2019**, *157*, 382–391.

18. Jiang, C.; Xie Y.; Kong, C.; Zhang, J.; Young D.J. Corrosion behaviour of Ni-Cr alloys in mixed oxidising gases at 650 °C. *Corros. Sci.* **2020**, *174*, 108801.

19. Xing, X.; Li, Z.X., Li, M.; Zhou C. Comparison of the corrosion resistance of Ni2Al3 coating with and without Ni-Re interlayer in dry and wet CO2 gas. *Corros. Sci.* **2019**, *159*, 108121.

20. Ai, H.; Yea, X.X.; Jiang, L.; Lenga, B.; Shen, M.; Li, Z.; Jia, Y.; Wang, J.Q.; Zhou, X.; Xie, Y.; Xie, L. On the possibility of severe corrosion of a Ni-W-Cr alloy influoride moltensalts at high temperature. *Corros. Sci.* **2019**, *149*, 218–225.

21. Chmielewski, M.; Pietrzak, K.; Basista, M.; Weglewski, W. Rhenium doped chromium–alumina composites for high-temperature applications. *Int. J. Refract. Met. Hard Mater.* **2016**, *54*, 196–202.

22. Petrovich, V.; Haurylau, M.; Volchek, S. Rhenium deposition on silicon surface at the room temperature for application in microsystems. *Sens. Actuator* **2002**, *99*, 45–48.

23. Kojima, R.; Enomoto, H.; Muhler, M.; Aika, K. Cesium-promoted rhenium catalysts supported on alumina for ammonia synthesis. *Appl. Catal. A Gen.* **2003**, *246*, 311–322.

24. Roger, J.; Audubert, F.; Petitcorps Y.L. Thermal reactions of SiC films with Mo, Re and Mo-Re alloys. *J. Alloy Compd.* **2009**, *475*, 635–642.

25. Kindrachuk, V.; Wanderka, N.; Banhart, J.; Mukherji, D.; Del Genovese, D.; Rösler, J. Effect of rhenium addition on the microstructure of the superalloy Inconel 706. *Acta Mater.* **2008**, *56*, 1609–1618.

26. Brynk, T.; Pakiela, Z.; Ludwichowska, K.; Romelczyk, B.; Molak, R.M.; Plocinska, M.; Kurzac, J.; Kurzynowski, T.; Chlebus, E. Fatigue crack growth rate and tensile strength of Re modified Inconel 718 produced by means of selective laser melting. *Mat. Sci. Eng. A Struct.* **2017**, *698*, 289–301.

27. Yoon, K.E.; Noebe, R.D.; Seidman, D.N. Effects of rhenium addition on the temporal evolution of the nanostructure and chemistry of a model Ni-Cr-Al superalloy. I: Experimental observations. *Acta Mater.* **2007**, *55*, 1145–1157.

28. Yoon, K.E.; Noebe, R.D.; Seidman, D.N. Effects of rhenium addition on the temporal evolution of the nanostructure and chemistry of a model Ni–Cr–Al superalloy. II: Analysis of the coarsening behaviour. *Acta Mater.* **2007**, *55*, 1159–1169.

29. Bochenek, K.; Węglewski, W.; Morgiel, J.; Maj, M.; Basista, M. Enhancement of fracture toughness of hot-pressed NiAl-Re material by aluminum oxide addition. *Mat. Sci. Eng. A Struct.* **2020**, *790*, 139670-1-6.

30. Kruszewski, M.J.; Zybała, R.; Ciupinski, Ł.; Chmielewski, M.; Adamczyk-Cieślak, B.; Michalski, A.; Rajska, M.; Kurzydłowski, K.J. Microstructure and thermoelectric properties of bulk cobalt antimonide (CoSb3) skutterudites obtained by pulse plasma sintering. *J. Electron. Mater.* **2016**, *45*, 1369–1376.

31. Orru, R.; Licheri, R.;. Locci, A.M.; Cincotti, A.; Cao, G. Consolidation/synthesis of materials by electric current activated/assisted sintering. *Mat. Sci. Eng. R.* **2009**, *63*, 127–287.

32. Chmielewski, M.; Pietrzak, K.; Teodorczyk, M.; Nosewicz, S.; Jarząbek, D.; Zybała, R.; Bazarnik, P.; Lewandowska, M.; Strojny-Nędza, A. Effect of metallic coating on the properties of copper-silicon carbide composites. *Appl. Surf. Sci.* **2017**, *421A*, 159–169.

33. Caron, P.; Khan, T. Evolution of Ni-based superalloys for single crystal gas turbine blade applications. *Aerosp. Sci. Technol.* **1999**, *3*, 513–523.

34. Osório, W.R.; Peixoto, L.C.; Canté, M.V.; Garcia, A. Electrochemical corrosion characterization of Al-Ni alloys in a dilute sodium chloride solution. *Electrochim. Acta* **2010**, *55*, 4078–4085.

35. Sun, Y.; Li, C.; Yu, L.; Gao, Z., Xia, X.; Liu, Y. Corrosion behavior of Al-15%Mg2Si alloy with 1% Ni addition. *Results Phys.* **2020**, *17*, 103129.

36. Deo, Y.; Guha, S.; Sarkar, K.; Mohanta, P.; Pradhan, D.; Mondal, A. Electrodeposited Ni-Cu alloy coatings on mild steel for enhanced corrosion properties. *Appl. Surf. Sci.* **2020**, *515*, 146078.

37. Liu, S.; Xia, C.; Yang, T.; Yang, Z.; Liu, N.; Li, Q. High strength and superior corrosion resistance of the Ti-Ni-Cu-Zr crystal/glassy alloys with superelasticity. *Mater. Lett.* **2020**, *260*, 126938.

38. Li, Y.; Wei, S.; Cheng, X.; Zhang, T.; Cheng, G. Corrosion behavior and surface characterization of tantalum implanted TiNi alloy. *Surf. Coat. Technol.* **2008**, *202*, 3017–3022.

39. Cheng, Y.; Zheng, Y.F. The corrosion behavior and hemocompatibility of TiNi alloys coated with DLC by plasma based ion implantation. *Surf. Coat. Technol.* **2006**, *200*, 4543–4548.

40. Fu, Y.; Wu, X.; Wang, Y.; Li, B.; Yang, S.Z. Study of corrosion resistance property and microstructure of TiNi shape memory alloy modified by pulsed high-energy density plasma. *Appl. Surf. Sci.* **2000**, *157*, 167–177.

41. Kanyane, L.R.; Adesina, O.S.; Popoola, A.P.I.; Farotade, G.A.; Malatji, N. Microstructural evolution and corrosion properties of laser clad TiNi on titanium alloy (Ti6Al4V). *Procedia Manuf.* **2019**; *35*, 1267–1272.

42. Chmielewski, M.; Pietrzak, K. Processing, microstructure and mechanical properties of Al2O3-Cr nanocomposites. *J. Eur. Ceram. Soc.* **2007**, *27*, 1273–1279.